Syracuse University

SURFACE

12-21-2004

Fixed-Connectivity Membranes

Mark Bowick
Department of Physics, Syracuse University, Syracuse, NY

Recommended Citation

Fixed-Connectivity Membranes

Mark Bowick

Department of Physics, Syracuse University, Syracuse, NY 13244-1130, USA.

The statistical mechanics of flexible surfaces with internal elasticity and shape fluctuations is summarized. Phantom and self-avoiding isotropic and anisotropic membranes are discussed, with emphasis on the universal negative Poisson ratio common to the low-temperature phase of phantom membranes and all strictly self-avoiding membranes in the absence of attractive interactions. The study of crystalline order on the frozen surface of spherical membranes is also treated.

I. INTRODUCTION

The statistical mechanics of polymers, which are *one-dimensional* chains or loops to a first approximation, has proven to be a rich and fascinating field.[1, 2, 3] The success of physical methods applied to polymers relies on universality – many of the macroscopic length scale properties of polymers are independent of microscopic details such as the chemical identity of the monomers and their interaction potential.[4]

Membranes are two-dimensional (2D) generalizations of polymers. The generalization of polymer statistical mechanics to membranes, surfaces fluctuating in three dimensions, has proven to be very rich because of the richer spectrum of shape and elastic deformations available. In contrast to polymers, there are *distinct* universality classes of membranes distinguished by the nature of their short-range order. There are crystalline, fluid and hexatic membrane analogues of the corresponding phases of strictly two-dimensional systems (monolayers) where shape fluctuations are frozen.[5, 6, 7]
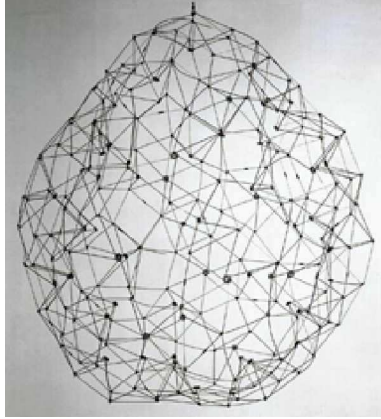

FIG. 1: Esfera (Sphere) 1976: Gertrude Goldschmidt (Gego). Stainless steel wire - 97 × 88 cm (Patricia Phelps de Cisneros Collection, Caracas, Venezuela).

The closest membrane analogue to a polymer is a 2D fishnet-like mesh of nodes with a fixed coordination number for each node. A fixed-connectivity membrane with spherical topology from the world of art[8] is shown in Fig.1. Bonds are assumed to be unbreakable while the nodes themselves live in flat d-dimensional Euclidean space $\mathbf{R}^d$, with a physical membrane corresponding to the case $d = 3$. The intrinsic crystalline order of fixed-connectivity membranes with, say, typical coordination number 6, leads to the alternative terminology crystalline membranes. They are also referred to as polymerized or tethered membranes. In general the Hamiltonian for a fixed-connectivity membrane will include both intrinsic elastic contributions (compression and shear) and shape (bending) contributions, since the membrane undergoes both types of deformation.[9, 10]

Flexible membranes are an important member of the enormous class of *soft* condensed matter systems.[3, 11, 12, 13] Soft matter responds easily to external forces and has physical properties that are often dominated by the entropy of thermal or other statistical fluctuations.

This chapter will describe the properties of fixed-connectivity membranes with focus on the universal negative Poisson ratio that illustrates the novel elastic behavior of the extended (*flat*) phase of physical membranes, the tubular phase of anisotropic membranes and ordering on frozen curved membrane topographies.

II. PHYSICAL EXAMPLES OF MEMBRANES

One can polymerize suitable chiral oligomeric precursors to form molecular sheets.[14] This approach is based directly on the idea of creating an intrinsically two-dimensional polymer. Alternatively one can permanently cross-link fluid-like Langmuir-Blodgett films or amphiphilic layers by adding certain functional groups to the hydrocarbon tails and/or the polar heads,[15, 16] as shown schematically in Fig.2.
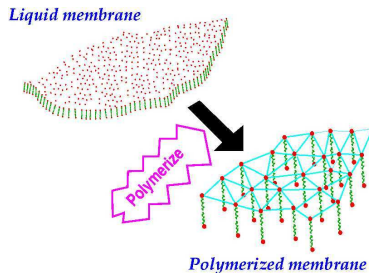

FIG. 2: Making a fixed-connectivity membrane by polymerizing a fluid membrane.
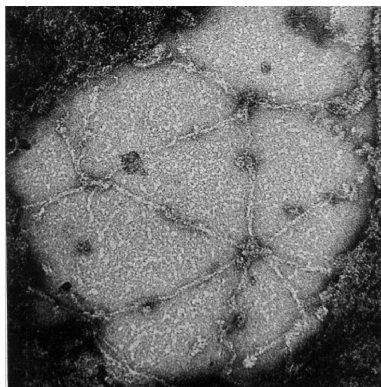

FIG. 3: An electron micrograph of a 0.5 micron square region of a red blood cell cytoskeleton at magnification 365,000:1. The skeleton is negatively stained and has been artificially spread to a surface area nine to ten times as great as in the native membrane. Image courtesy of Daniel Branton (Dept. of Biology, Harvard University).

The 2D-cytoskeletons of certain cell membranes are beautiful and naturally occurring fixed-connectivity membranes that are essential to the function and stability of the cell as a whole.[17, 18, 19, 20, 21] The simplest and most thoroughly studied example is the cytoskeleton of mammalian erythrocytes (red blood cells). The human body has roughly 5×10^{13} red blood cells. The red blood cell cytoskeleton is a protein network whose links are spectrin tetramers (of length approximately 200 nm) meeting at junctions composed of short actin filaments (of length 37 nm and typically 13 actin monomers long)[22, 23, 24] (see Fig.3 and Fig.4). There are roughly 70,000 triangular faces in the entire mesh which is bound as a whole by ankyrin and other proteins to the cytoplasmic side of the other key component of the cell membrane, the fluid phospholipid bilayer. Without the cytoskeleton the lipid bilayer would disintegrate into a thousand little vesicles and certainly the red blood cell would not be capable of the shape deformations required to squeeze through narrow capillaries.

There are also inorganic realizations of fixed-connectivity membranes. Graphitic oxide (GO) membranes are micron size sheets of solid carbon, with thicknesses on the order of 10Å, formed by exfoliating carbon with a strong oxidizing agent. Their structure in an aqueous suspension has been examined by several groups.[25, 26, 27] Metal dichalcogenides such as MoS_2 have also been observed to form rag-like sheets.[28] Finally similar structures occur in the large sheet molecules, shown in Fig.5, and believed to be an ingredient in glassy B_2O_3.

III. PHASE DIAGRAMS

Let us consider the general class of D-dimensional elastic and flexible manifolds fluctuating in d-dimensional Euclidean space. Such manifolds are described by a d-dimensional vector $\vec{r}(\mathbf{x})$, where $\mathbf{x}$ labels the D-dimensional internal
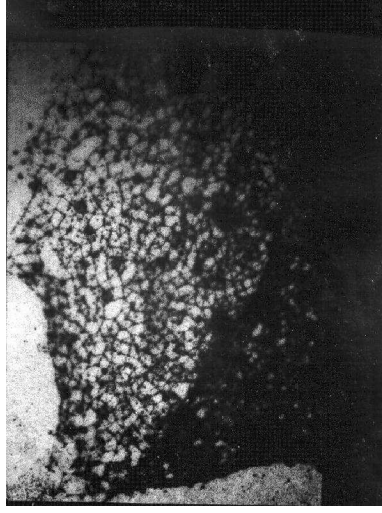
FIG. 4: An extended view of the spectrin/actin network which forms the cytoskeleton of the red blood cell membrane. Image courtesy of Daniel Branton.
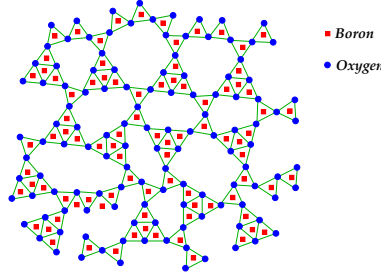

FIG. 5: The sheet molecule B_2O_3.

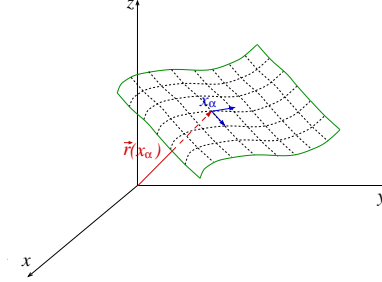coordinates, as illustrated in Fig.6. A physical membrane, of course, corresponds to the case $(D = 2, d = 3)$.

FIG. 6: The parametrization of a *membrane* with internal coordinates $\mathbf{x}$ and bulk coordinates $\vec{r}(\mathbf{x})$.

The Landau free energy of a membrane must be invariant under global translations, so the order parameter is given by derivatives of the embedding $\vec{r}$, viz. the tangent vectors $\vec{t}_\alpha = \frac{\partial \vec{r}}{\partial x^\alpha}$, with $\alpha = 1, \cdots, D$. Invariance under rotations in both the internal and bulk space limits the Landau free energy to the form [5, 29, 30]

$$
\begin{aligned}
F(\vec{r}) &= \int d^D\mathbf{x} \left[\frac{t}{2}(\partial_\alpha\vec{r})^2 + u(\partial_\alpha\vec{r}\partial_\beta\vec{r})^2 + v(\partial_\alpha\vec{r}\partial^\alpha\vec{r})^2 + \frac{\kappa}{2}(\partial^2\vec{r})^2 \right] \\
&+ \frac{b}{2}\int d^D\mathbf{x}\,d^D\mathbf{y}\,\delta^d\left(\vec{r}(\mathbf{x}) - \vec{r}(\mathbf{y})\right) \ ,
\end{aligned}
\tag{1}
$$

where higher order terms are irrelevant in the long wavelength limit. The physics of Eq.(1) depends on the elastic

moduli t, u and v, the bending rigidity κ and the strength of self-avoidance b. The limit $b = 0$ describes a *phantom* membrane that may self-intersect with no energy cost.

For small deformations from a reference ground state one may write $\vec{r}(\mathbf{x})$ as

$$\vec{r}(\mathbf{x}) = \left(\zeta\mathbf{x} + \mathbf{u}(\mathbf{x}), \vec{h}(\mathbf{x})\right) , \tag{2}$$

where $\mathbf{u}(\mathbf{x})$ are D "internal" phonon modes and $\vec{h}(\mathbf{x})$ $d - D$ "out-of-plane" height fluctuations. The case $\zeta = 0$ corresponds to a mean field isotropic crumpled phase for which typical equilibrium membrane configurations have fractal Hausdorff dimension d_H ($d_H = \infty$ for phantom membranes) and there is no distinction between the internal phonons and the height modes. The crumpled phase is illustrated in Fig.7(a).

The regime $\zeta \neq 0$ describes a membrane which is "flat" up to small fluctuations. The full rotational symmetry of the free energy is spontaneously broken. The fields $\vec{h}$ are the Goldstone modes and scale differently than the phonon fields $\mathbf{u}$. Fig.7(c) is a visualization of a typical configuration in the "flat" phase.
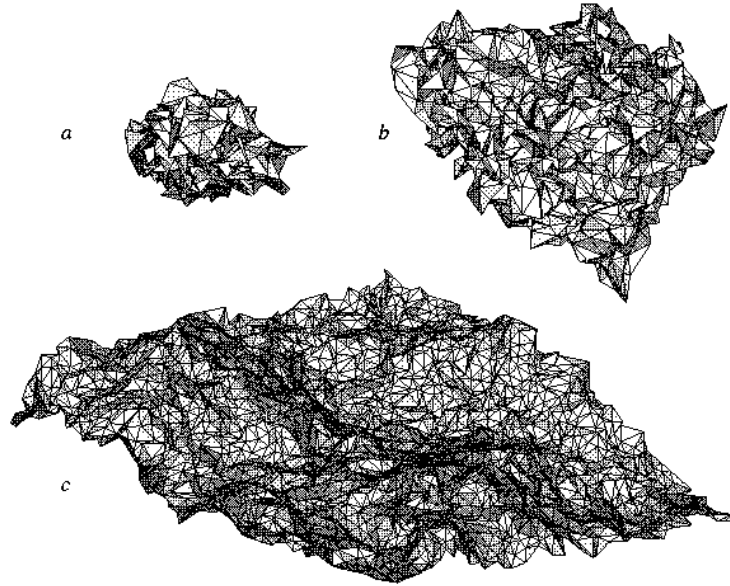

FIG. 7: Typical configurations of phantom membranes: (a) the crumpled phase, (b) the critical *crumpling* phase and (c) the *flat* or bulk-orientationally-ordered phase. Images are from the simulations of Ref.31.

Phantom membranes are by far the easiest to treat analytically and numerically. They may even be physically realizable by synthesizing membranes from strands that cut and repair themselves on a sufficiently short time scale that they access self-intersecting configurations. One can also view the analysis of the phantom membrane as the first step in understanding the more physical self-avoiding membrane. Combined analytical and numerical studies have yielded a thorough understanding of the phase diagram of phantom fixed-connectivity membranes.

A.   Phantom Membranes

The phantom membrane free energy is

$$F(\vec{r}) = \int d^D\mathbf{x} \left[\frac{t}{2}(\partial_\alpha\vec{r})^2 + u(\partial_\alpha\vec{r}\partial_\beta\vec{r})^2 + v(\partial_\alpha\vec{r}\partial^\alpha\vec{r})^2 + \frac{\kappa}{2}(\partial^2\vec{r})^2\right] . \tag{3}$$

The mean field effective potential, using the expansion of Eq.(2), is

$$V(\zeta) = D\zeta^2 \left(\frac{t}{2} + (u + vD)\zeta^2\right) , \tag{4}$$

with minima

$$\zeta^2 = \begin{cases} 0 & : \quad t \geq 0 \\ -\frac{t}{4(u+vD)} & : \quad t < 0 \end{cases}.$$ (5)

This implies a "flat" (extended) phase for $t < 0$ and a crumpled phase for $t > 0$, separated by a continuous crumpling transition at $t = 0$, as sketched in Fig.8.
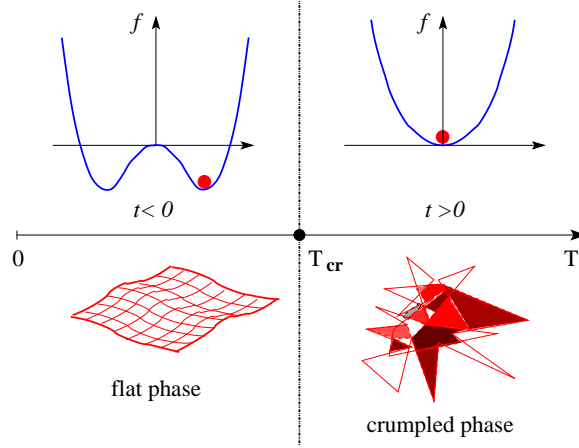

FIG. 8: The mean field free energy density f of fixed-connectivity membranes as a function of the order parameter t together with a schematic of the low temperature flat ordered phase and the high temperature crumpled disordered phase.

Of course anything is possible in mean field theory but a variety of analytic and numerical calculations indicates the true phase diagram of phantom membranes is qualitatively like Fig.9.[9] The crumpled phase is described by a line of equivalent Gaussian fixed points (GFPs). There is a crumpling transition line in the $\kappa - t$ plane containing an infrared stable fixed point (CTFP) which describes the long wavelength properties of the crumpling transition. Finally, for large enough values of κ and negative values of t, the system is in a "flat" phase whose properties are dictated by an infrared stable flat phase fixed point (FLFP).
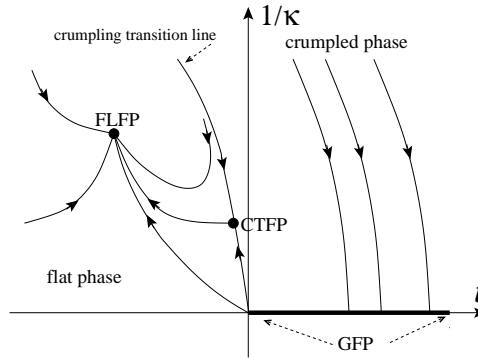

FIG. 9: Schematic plot of the phase diagram for phantom membranes.

1. The crumpled phase

In the crumpled phase, the free energy Eq.(3), for $D \geq 2$, simplifies to

$$F(\vec{r}) = \frac{t}{2} \int d^D \mathbf{x} \, (\partial_\alpha \vec{r})^2 + \text{irrelevant terms} ,$$ (6)

since the model is completely equivalent to a linear sigma model with $O(d)$ internal symmetry in $D \geq 2$ dimensions and therefore all derivative operators in $\vec{r}$ are irrelevant by power counting.[32, 33] The parameter t labels equivalent gaussian fixed points, as depicted in Fig.9. In renormalization group language there is a marginal direction for positive t. The large distance properties of this phase are described by simple gaussian fixed points with the exact connected 2-point function:

$$G(\mathbf{x}) \sim \begin{cases} |\mathbf{x}|^{2-D} & : D \neq 2 \\ \log |\mathbf{x}| & : D = 2 \end{cases} \tag{7}$$

The associated critical exponents may also be computed exactly. The Hausdorff (fractal) dimension d_H, or equivalently the size exponent $\nu = D/d_H$, is given (for the physical case $D = 2$) by

$$d_H = \infty \ (\nu = 0) \Rightarrow R_G^2 \sim \log L , \tag{8}$$

where R_G^2 is the radius of gyration and L is the linear membrane size. This result is confirmed by numerical simulations of fixed-connectivity membranes in the crumpled phase where the logarithmic behavior of the radius of gyration is accurately checked.[31]·[34]⁻[45]

2. The Crumpling Transition

Near the crumpling transition the membrane free energy is given by

$$F(\vec{r}) = \int d^D \mathbf{x} \left[\frac{1}{2} (\partial^2 \vec{r})^2 + u (\partial_\alpha \vec{r} \partial_\beta \vec{r})^2 + \hat{v} (\partial_\alpha \vec{r} \partial^\alpha \vec{r})^2 \right] , \tag{9}$$

where the bending rigidity has been scaled out and $\hat{v} = v - \frac{u}{D}$. By naive power counting the directions defined by the couplings u and $\hat{v}$ are relevant for $D \leq 4$ and the model is amenable to an $\varepsilon = 4 - D$-expansion. The β functions are given by[9]

$$\beta_u(u_R, v_R) = -\varepsilon u_R + \frac{1}{8\pi^2} \left\{ \left(\frac{d}{3} + \frac{65}{12} \right) u_R^2 + 6 u_R v_R + \frac{4}{3} v_R^2 \right\} \tag{10}$$

and

$$\beta_v(u_R, v_R) = -\varepsilon v_R + \frac{1}{8\pi^2} \left\{ \frac{21}{16} u_R^2 + \frac{21}{2} u_R v_R + (4d + 5) v_R^2 \right\} . \tag{11}$$

These two coupled beta functions have a fixed point only for $d > 219$.[29] This suggests that the crumpling transition is first order for $d = 3$. Other analyses, however, indicate a continuous crumpling transition. A revealing extreme limit of membranes was studied by David and Guitter.[46] This is the limit of infinite elastic constants in the flat phase. Since the elastic terms in the Hamiltonian scale like q^2 in momentum space, as compared to q^4 for the bending energy, this limit exposes the dominant infrared behavior of the membrane. In this "stretchless" limit the elastic strain tensor $u_{\alpha\beta}$ must vanish and the Hamiltonian is constrained, very much in analogy to a nonlinear sigma model. The Hamiltonian becomes

$$H_{NL} = \int d^D \sigma \frac{\kappa}{2} (\Delta \vec{r})^2 , \tag{12}$$

together with the constraint $\partial_\alpha \vec{r} \partial_\beta \vec{r} = \delta_{\alpha\beta}$. Remarkably, the β-function for the inverse bending rigidity $\alpha = 1/\kappa$ may be computed within a large-d expansion, giving

$$\beta(\alpha) = q \frac{\partial \alpha}{\partial q} = \frac{2}{d} \alpha - \left(\frac{1}{4\pi} + \frac{\text{const.}}{d} \right) \alpha^2 . \tag{13}$$

For $d = \infty$ there is no stable fixed point and the membrane is always crumpled. To next order in $1/d$, however, Eq.(13) reveals an ultraviolet stable fixed point at $\alpha = 8\pi/d$, corresponding to a continuous crumpling transition. The size exponent at the transition is found to be[47]

$$d_H = \frac{2d}{d-1} \implies \nu = 1 - \frac{1}{d} = 2/3 \text{ (for } d = 3) . \tag{14}$$

Le Doussal and Radzihovsky[48] analyzed the Schwinger-Dyson equations for the model of Eq.(9) keeping up to four point vertices. The result for the Hausdorff dimension and size exponent is

$$d_H = 2.73 \implies \nu = 0.73 . \tag{15}$$

Finally Monte Carlo Renormalization Group simulations[49] of the crumpling transition find a continuous transition with exponents

$$d_H = 2.77(10) \qquad \nu = 0.71(3) \tag{16}$$

Thus three independent   size exponent.
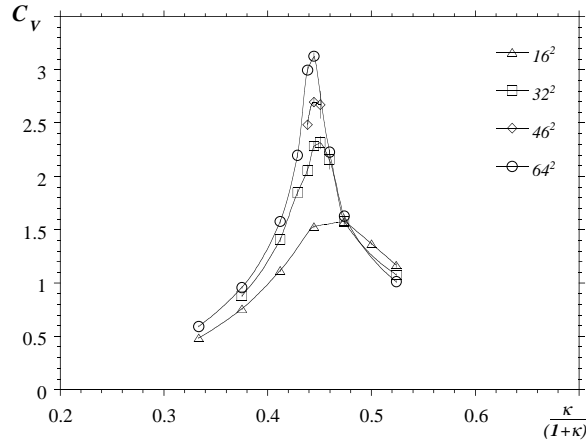
FIG. 10: Plot of the specific heat observable from the simulations of Ref.31. The growth of the specific heat peak with system size indicates a continuous transition.

Further evidence for the crumpling transition being continuous is provided by numerous numerical simulations[9, 44, 45] where the analysis of observables like the specific heat (see Fig.10) or the radius of gyration radius give textbook continuous phase transitions, although the value of the exponents at the transition are difficult to determine precisely.

3.   The Flat Phase

FIG. 11: Membrane coordinates appropriate for analyzing fluctuations in the flat phase.

In a flat membrane (see Fig.11), it is natural to introduce the strain tensor

$$u_{\alpha\beta} = \partial_\alpha u_\beta + \partial_\beta u_\alpha + \partial_\alpha h \partial_\beta h . \tag{17}$$

The free energy Eq.(3) in these variables becomes

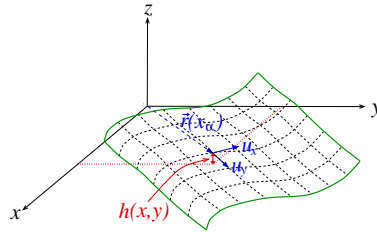$$F(\mathbf{u}, h) = \int d^D \mathbf{x} \left[\frac{\hat{\kappa}}{2} (\partial_\alpha \partial_\beta h)^2 + \mu u_{\alpha\beta} u^{\alpha\beta} + \frac{\lambda}{2} (u_\alpha^\alpha)^2 \right] , \tag{18}$$

where irrelevant higher derivative terms have been dropped. One recognizes the standard Landau free energy of elasticity theory,[50] with Lamé coefficients μ and λ, plus an extrinsic curvature term, with bending rigidity $\hat{\kappa}$. These couplings are related to the original ones in Eq.(3) by $\mu = u\zeta^{4-D}$, $\lambda = 2v\zeta^{4-D}$, $\hat{\kappa} = \kappa\zeta^{4-D}$ and $t = -4(\mu + \frac{D}{2}\lambda)\zeta^{D-2}$. The large distance properties of the flat phase for fixed-connectivity membranes are completely described by the free energy of Eq.(18). Since the bending rigidity may be scaled out at the crumpling transition, the free energy becomes a function of $\frac{\mu}{\kappa^2}$ and $\frac{\lambda}{\kappa^2}$. The β-functions for the couplings μ and λ in the ε-expansion are[51, 52]

$$\beta_\mu(\mu_R, \lambda_R) = -\varepsilon\mu_R + \frac{\mu_R^2}{8\pi^2} \left(\frac{d_c}{3} + 20A \right) ; \tag{19}$$

$$\beta_\lambda(\mu_R, \lambda_R) = -\varepsilon\lambda_R + \frac{1}{8\pi^2} \left(\frac{d_c}{3}\mu_R^2 + 2(d_c + 10A)\lambda_R\mu_R + 2d_c\lambda_R^2 \right) ,$$

where d_c is the codimension $d - D$ and $A = \frac{\mu_R + \lambda_R}{2\mu_R + \lambda_R}$. These coupled β-functions possess four fixed points (see Fig.12) whose values are shown in Table I.
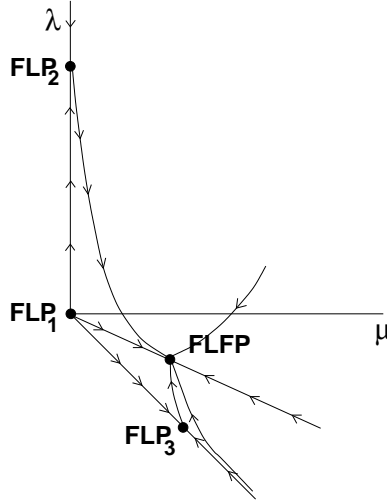
FIG. 12: Phase diagram for the phantom flat phase. There are three infra-red unstable fixed points, labelled by FLP1, FLP2 and FLP3, but the physics of the flat phase is governed by the infra-red stable fixed point (FLFP).

The phase diagram revealed by the ε-expansion is thus a little more complex than that sketched in Fig.9. The three additional fixed points are infra-red unstable, however, and can only be reached for very specific values of the Lamé coefficients.

4. The properties of the flat phase

Fig.7(c) shows a typical equilibrium configuration for a membrane that has developed a preferred orientation in the bulk - the surface normals clearly have long-range order. In this phase the membrane is a rough extended two-dimensional structure. The rotational symmetry of the full free energy is spontaneously broken from $O(d)$ to $O(d - D) \times O(D)$. The remnant rotational symmetry is realized in Eq.(18) as

$$h_i(\mathbf{x}) \ \rightarrow \ h_i(\mathbf{x}) + A^{i\alpha}\mathbf{x}_\alpha \ ; \tag{20}$$
$$u_\alpha(\mathbf{x}) \ \rightarrow \ u_\alpha - A^{i\alpha}h_i - \frac{1}{2}\delta^{ij}A^{i\alpha}A^{\beta j}\mathbf{x}_\beta \ ,$$

where $A^{i\alpha}$ is a $D \times (d-D)$ matrix. This relation provides Ward identities which greatly simplify the renormalization of the theory.

The phonon and height propagators in the infrared limit are given by

$$\Gamma_{uu}(\vec{p}) \ \sim \ |\vec{p}|^{2+\eta_u} \ ; \tag{21}$$
$$\Gamma_{hh}(\vec{p}) \ \equiv \ |\vec{p}|^4 \kappa(\vec{p}) \sim |\vec{p}|^{4-\eta} \ ,$$

where the last equation defines the anomalous bending rigidity $\kappa(\vec{p}) \sim |\vec{p}|^{-\eta}$. The two scaling exponents η_u and η are related by the scaling relation[51]

$$\eta_u = 4 - D - 2\eta \ , \tag{22}$$

which follows from the Ward identities (Eq.(20)) associated with the remnant rotational symmetry . The roughness exponent ζ, which measures the growth with system size of the rms height fluctuations transverse to the flat directions, is determined from η by the further scaling relation

$$\zeta = \frac{4 - D - \eta}{2} \ . \tag{23}$$

The long wavelength properties of the flat phase are described by the FLFP (see Fig.12). Since the FLFP occurs at non-zero renormalized values of the Lamé coefficients, the associated critical exponents are clearly non-Gaussian. These key critical exponents have also been determined by independent methods.

Large scale simulation of membranes in the flat phase model were performed in Ref.[31] The results obtained for the critical exponents are very accurate:

$$\eta_u = 0.50(1) \, ; \ \ \eta = 0.750(5) \, ; \ \ \zeta = 0.64(2) \, . \tag{24}$$

A review of numerical results may be found in Refs.[44, 45].

The SCSA approximation[48] gives a beautiful result for general d:

$$\eta(d) = \frac{4}{d_c + \sqrt{16 - 2d_c + d_c^2}} \ , \tag{25}$$

which for $d = 3$ gives

$$\eta_u = 0.358 \, ; \ \ \eta = 0.821 \, ; \ \ \zeta = 0.59 \, . \tag{26}$$

Finally the large-d expansion[46] gives

$$\eta = \frac{2}{d} \ \Longrightarrow \ \eta(3) = 2/3 \ . \tag{27}$$

TABLE I: The fixed points and critical exponents of the flat phase.

FP	μ_R^*	λ_R^*	η	η_u
FLP1	0	0	0	0
FLP2	0	$2\varepsilon/d_c$	0	0
FLP3	$\frac{12\varepsilon}{20+d_c}$	$\frac{-6\varepsilon}{20+d_c}$	$\frac{\varepsilon}{2+d_c/10}$	$\frac{\varepsilon}{1+20/d_c}$
FLFP	$\frac{12\varepsilon}{24+d_c}$	$\frac{-4\varepsilon}{24+d_c}$	$\frac{\varepsilon}{2+d_c/12}$	$\frac{\varepsilon}{1+24/d_c}$

The numerical simulations are in qualitative agreement with both the SCSA and large-d analytical estimates.

On the experimental side we are fortunate to have two measurements of the key critical exponents for the flat phase of fixed-connectivity membranes. The static structure factor of the red blood cell cytoskeleton has been measured by small-angle x-ray and light scattering, yielding a roughness exponent of $\zeta = 0.65(10)$.[24] Freeze-fracture electron microscopy and static light scattering of the conformations of graphitic oxide sheets reveal flat sheets with a fractal dimension $d_H = 2.15(6)$. Both these measured values are in good agreement with the best analytic and numerical predictions, but the errors are still too large to discriminate between different analytic calculations and to accurately substantiate the numerical simulations.

The Poisson ratio[50] of a phantom fixed-connectivity membrane (which measures the transverse elongation due to a longitudinal stress) is universal and within the SCSA approximation is given by

$$\sigma(D) = -\frac{1}{D+1} \implies \sigma(2) = -1/3 \ . \tag{28}$$

This result has also been checked in numerical simulations.[53, 54] Rather remarkably, it turns out to be negative. While Ref.[53] finds $\sigma \approx -0.15$ the latter simulation[54] finds $\sigma \approx -0.32$. Materials with a negative Poisson ratio have been dubbed *auxetics*[55]. The wide variety of potential applications of auxetic materials suggests a fascinating role for flexible fixed-connectivity membranes in materials science (see Sect. IV).

A final critical regime of a flat membrane is achieved by subjecting the membrane to external tension.[47] This gives rise to a low temperature phase in which the membrane has a domain structure, with distinct domains corresponding to flat phases with different bulk orientations. This describes, physically, a *buckled* membrane whose equilibrium shape is no longer planar.

B.   Self-avoiding Membranes

Physically realistic fixed-connectivity membranes will have large energy barriers to self-intersection. That is they will generally be self-avoiding. Self-avoidance is familiar in the physics of polymer chains and may be treated by including the Edwards-type delta-function repulsion of the Hamiltonian in Eq.(1). A detailed summary of our current understanding is given in Refs.[9, 10] The essential finding is that self-avoidance eliminates all but the flat phase.

1.   Numerical simulations

Numerical simulations are currently essential in understanding the statistical mechanics of self-avoiding membranes because the treatment of nonlinear elasticity together with non-local self-avoidance is currently beyond the realm of analytic techniques.

Two discretizations of membranes have been adopted to incorporate self-avoidance. The *balls and springs* class of models begins with a network of N particles in a intrinsically triangular array and interacting via a nearest-neighbor elastic potential

$$V_{NN}(\vec{r}) = \begin{cases} 0 & \text{for } |\vec{r}| \leq b \\ \infty & \text{for } |\vec{r}| > b \end{cases} , \tag{29}$$

where the free parameter b plays the role of a tethering length. An additional hard sphere steric repulsion forbids *any* node to be closer than a distance σ from any other node:

$$V_{steric}(\vec{r}) = \begin{cases} \infty & \text{for } |\vec{r}| \leq \sigma \\ 0 & \text{for } |\vec{r}| > \sigma \end{cases} . \tag{30}$$

Early simulations[34, 35] of this class of model gave a first estimate of the fractal dimension for physical membranes compatible with the Flory estimate $d_H = 2(d+D)/(2+D) = 2.5$.[36] The system sizes simulated, however, were quite small and subsequent simulations for larger systems found that the membrane is flat.[56, 57] This result is remarkable when one recalls that there is no explicit bending rigidity.

A plausible explanation[58] for the loss of the crumpled phase is that next-to-nearest neighbor excluded volume effects induce a positive bending rigidity, driving the model to the FLFP. The structure function of the self-avoiding

model has been computed numerically[59] and found to compare well with the analytical structure function for the flat phase of phantom fixed-connectivity membranes. In particular the roughness exponents are comparable.

The induced bending rigidity may be lowered by taking a smaller excluded volume.[60] The flat phase persists to very small values of σ with eventual signs of a crumpled phase, probably due to effective loss of self-avoidance. A more comprehensive study,[61] in which the hard sphere radius is taken to zero with an excluded volume potential which is a function of the internal distance along the lattice, concluded that self-avoidance implies flatness in the thermodynamic limit of large membranes.

Self-avoidance may also be implemented by modelling impenetrable triangular meshes. This has the advantage that there is no restriction on the bending angle between adjacent cells and therefore no induced bending rigidity.[62]

The first simulations of the plaquette model[63] found a Hausdorff dimension in rough agreement in agreement with the Flory estimate 2.5 but this has not held up in subsequent work. A subsequent simulation[64] found $d_H \approx 2.3$ and extensive recent work employing more sophisticated algorithms and extending to much larger membranes confirm the loss of the crumpled phase.[62]

Some insight into the lack of a crumpled phase for self-avoiding fixed-connectivity membranes is offered by the study of folding. [65]−[71] Folding corresponds to the limit of infinite elastic constants[46] with the further approximation that the space of bending angles is discretized. One quickly discovers that the reflection symmetries of the allowed folding vertices forbid local folding (crumpling) of surfaces. There is therefore essentially no entropy for crumpling. There is, however, local unfolding and the resulting statistical mechanical models are non-trivial. The lack of local folding is the discrete equivalent of the long-range curvature-curvature interactions that stabilize the flat phase. The dual effect of the integrity of the surface (time-independent connectivity) and self-avoidance is so powerful that crumpling seems to be impossible in low embedding dimensions.

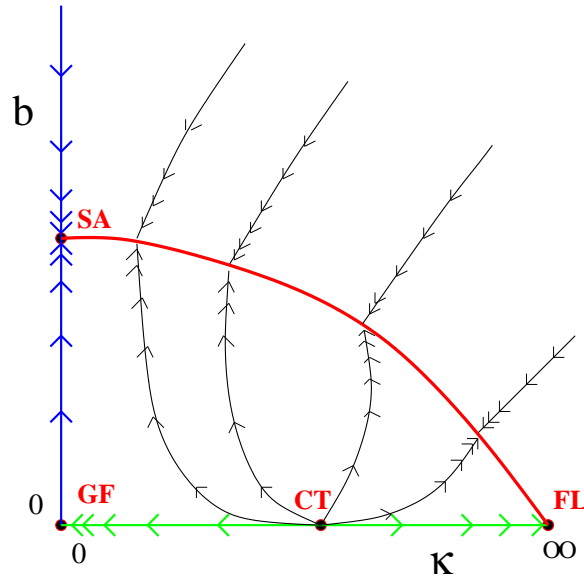### 2. The properties of the self-avoiding fixed point

FIG. 13: The conjectured phase diagram for self-avoiding fixed-connectivity membranes in 3 dimensions. With any degree of self-avoidance the renormalization group flows are to the flat phase fixed point of the phantom model (FL).

For the physically relevant case $d = 3$ numerical simulations thus find that there is no crumpled phase. Furthermore, the flat phase is *identical* to the flat phase of the phantom membrane.[62] The roughness exponent ζ_{SA} from numerical simulations of self-avoidance at $d = 3$ using ball-and-spring models[72] and impenetrable plaquette models[62] and the roughness exponent at the FLFP, Eq.(24), compare extremely well

$$\zeta_{SA} = 0.64(4) \ , \ \zeta = 0.64(2) \ . \tag{31}$$

The numerical evidence thus strongly indicates that the SAFP is exactly the same as the FLFP and that the crumpled self-avoiding phase is absent in the presence of purely repulsive potentials (see Fig.13). This conjecture is strengthened

by the finding that the Poisson ratio of self-avoiding membranes is the same as that of flat phantom membranes.[73] (see Sect.IV). This identification of fixed points enhances the significance of the FLFP treated earlier.

IV.   POISSON RATIO AND AUXETICS

In the classical theory of elasticity[50] an arbitrary deformation of a D-dimensional elastic body may be decomposed into a pure shear and a pure compression:

$$u_{ij} = [u_{ij} - \frac{1}{D}(\text{Tr}\,u)\delta_{ij}] + \frac{1}{D}(\text{Tr}\,u)\delta_{ij} \ , \tag{32}$$

where Tr denotes the trace and the term in square brackets is a pure shear (volume-preserving but shape changing) while the second term is a pure compression (shape-preserving but volume-changing). The elastic free energy is then given by

$$F_{el} = \mu \left[u_{ij} - \frac{1}{D}(\text{Tr}\,u)\delta_{ij}\right]^2 + \frac{1}{2}K\left(\text{Tr}\,u\right)^2 \ , \tag{33}$$

where μ is the shear modulus and K is the bulk modulus. This free energy may be written equivalently as

$$F_{el} = \mu\,u_{ij}u_{ij} + \frac{1}{2}\lambda\left(\text{Tr}\,u\right)^2 \ , \tag{34}$$

with the elastic Lamé coefficient λ related to the bulk and shear moduli by

$$K = \lambda + \frac{2\mu}{D} \ . \tag{35}$$

For the physical membrane, $D = 2$, this reads $K = \lambda + \mu$. Thermodynamic stability requires that both K and μ be positive, otherwise the free energy could be spontaneously lowered by pure compressional or pure shear deformations, respectively.

The Poisson ratio σ is defined as the ratio of transverse contractile strain to longitudinal tensile strain for an elastic body subject to a uniform applied tension T. For tension applied uniformly in, say, the x-direction

$$\sigma = -\frac{\delta y/y}{\delta x/x} \ , \tag{36}$$

the Poisson ratio is easily found to be

$$\sigma = \frac{K - \mu}{K + \mu} \ , \tag{37}$$

for $D = 2$, and

$$\sigma = \frac{1}{2}\left(\frac{3K - 2\mu}{3K + \mu}\right) \tag{38}$$

for $D = 3$. Thermodynamic stability is only possible for $-1 \le \sigma \le 1$ for $D = 2$ and $-1 \le \sigma \le \frac{1}{2}$ for $D = 3$. The upper bounds (1 and 1/2 respectively) are approached for materials that have vanishing shear modulus compared to their bulk modulus (rubber-like) and the lower bounds (-1) for materials with negligible bulk modulus in comparison to their shear modulus ("anti-rubber")[74]. Clearly, the Poisson ratio may be negative (auxetic) for $K < \mu$ (D=2) and $K < \frac{2}{3}\mu$ (D=3). Most materials get thinner when stretched and fatter when squashed – auxetic materials are uncommon. The earliest known example, dating from more than a century ago, is that of a pyrite (FeS$_2$) crystal[75], which has a Poisson ratio, in certain crystallographic directions, of $\sigma \approx -0.14$. More recently, some isotropic polyester foams have been created with Poisson ratios as large as $\sigma \sim -0.7$[77, 78]. The potential of auxetic materials in materials science

is nicely reviewed in Ref.[79]. One of the rare naturally occurring auxetics is SiO$_2$ in its α-crystobalite phase.[80, 81] Cristobalite is one of the three distinct crystalline forms of SiO$_2$, together with quartz and tridymite. Its Poisson ratio reaches a maximum negative value of -0.5 in some directions, with orientationally-averaged values for single-phased aggregates of -0.16.

The underlying mechanism driving fixed-connectivity membranes auxetic ($\sigma = -1/3$) has schematic similarities to that illustrated in Fig.14. Submitting a membrane to tension will suppress its out-of-plane fluctuations, forcing it entropically to expand in both in-plane directions. More physically, the out-of-plane undulations renormalize the elastic constants (the Lamé coefficients), in such a way that the long-wavelength bulk modulus is less than the shear modulus, which is the signature of a two-dimensional auxetic material. The soft matter origin of the universal negative Poisson ratio of fixed-connectivity membranes provides a fundamentally new paradigm for the design of novel materials. The best current experimental measurements of the Poisson ratio of the red blood cell cytoskeleton[82] find $\sigma \approx +1/3$ from separate determinations of the bulk and shear modulus. The cytoskeleton still has the fluid lipid bilayer attached, however, and this may influence the pure cytoskeletal elasticity. A direct measurement of the Poisson ratio for a flexible fixed-connectivity membrane remains an important and challenging task.
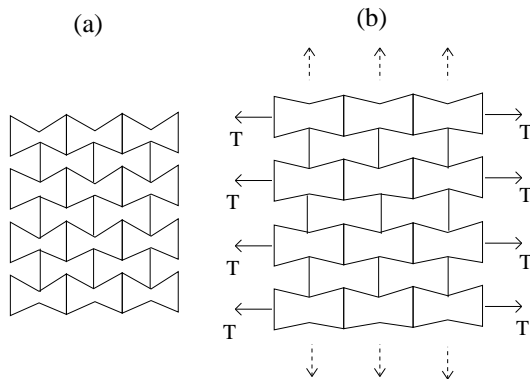

FIG. 14: Mechanical model of an auxetic material: (a) in the absence of applied stress and (b) under applied lateral stress T. The lateral stretching accompanying the applied stress forces the material out in the transverse dimension.

Auxetic materials have desirable mechanical properties such as higher in-plane indentation resistance, transverse shear modulus and bending stiffness. They have clear applications as sealants, gaskets and fasteners. They may also be promising materials for artificial arteries, since they can expand to accommodate sudden increases in blood flow.

We can model a realistic fixed-connectivity membrane with an elastic free energy and either large bending rigidity or self-avoidance. This is of practical importance in modelling since, for example, we may replace the more complicated non-local self-avoidance term with a large bending rigidity.

It would be very interesting to know if nature utilizes the auxetic character of the red-blood cell spectrin cytoskeleton in the elastic deformations of red blood cells as they pass through fine blood capillaries. As such cells deform, the membrane skeleton can unfold, which might help to transport large molecules or expose reactive chemical groups.[83]

V. ANISOTROPIC MEMBRANES

An anisotropic membrane is a fixed-connectivity membrane in which the elastic moduli or the bending rigidity in one distinguished direction are different from those in the remaining $D-1$ directions. Such a membrane may be described by a d-dimensional vector $\vec{r}(\mathbf{x}_\perp, y)$, where now the D dimensional internal coordinates are split into $D-1$ $\mathbf{x}_\perp$ coordinates and the orthogonal distinguished direction y.

Requiring invariance under translations, $O(d)$ rotations in the embedding space and $O(D-1)$ rotations in the internal space, the equivalent of Eq.(1) becomes

$$
\begin{aligned}
F\left(\vec{r}(\mathbf{x})\right) \;=\; & \frac{1}{2} \int d^{D-1}\mathbf{x}_\perp \, dy \left[\kappa_\perp (\partial_\perp^2 \vec{r})^2 + \kappa_y (\partial_y^2 \vec{r})^2 \right. \\
& + \kappa_{\perp y} \partial_y^2 \vec{r} \cdot \partial_\perp^2 \vec{r} + t_\perp (\partial_\alpha^\perp \vec{r})^2 + t_y (\partial_y \vec{r})^2 \\
& + \frac{u_{\perp\perp}}{2} (\partial_\alpha^\perp \vec{r} \cdot \partial_\beta^\perp \vec{r})^2 + \frac{u_{yy}}{2} (\partial_y \vec{r} \cdot \partial_y \vec{r})^2 \\
& + u_{\perp y}(\partial_\alpha^\perp \vec{r} \cdot \partial_y \vec{r})^2 + \frac{v_{\perp\perp}}{2}(\partial_\alpha^\perp \vec{r} \cdot \partial_\alpha^\perp \vec{r})^2 \\
& \left. + v_{\perp y}(\partial_\alpha^\perp \vec{r})^2 (\partial_y \vec{r})^2 \right] \\
& + \frac{b}{2} \int d^D\mathbf{x} \int d^D\mathbf{x}' \delta^d(\vec{r}(\mathbf{x}) - \vec{r}(\mathbf{x}')) \;.
\end{aligned}
\tag{39}
$$

This model has eleven free parameters – three distinct bending rigidities, $\kappa_\perp, \kappa_y$ and $\kappa_{\perp y}$, seven elastic moduli, $t_\perp, t_y, u_{\perp\perp}, u_{yy}, u_{\perp y}, v_{\perp\perp}$ and $v_{\perp y}$, and the strength of self-avoidance coupling b.

As before we decompose displacements as

$$
\vec{r}(\mathbf{x}) = \left(\zeta_\perp \mathbf{x}_\perp + \mathbf{u}_\perp(\mathbf{x}), \; \zeta_y y + u_y(\mathbf{x}), \; \vec{h}(\mathbf{x}) \right) \;,
\tag{40}
$$

with $\mathbf{u}_\perp$ being the $D-1$–dimensional intrinsic phonon modes, u_y the intrinsic phonon mode in the distinguished direction y and $\vec{h}$ the $d-D$-dimensional out-of-plane fluctuation mode. If $\zeta_\perp = \zeta_y = 0$, the membrane is crumpled and if both $\zeta_\perp$ and ζ_y do not vanish the membrane is flat. There is, however, the possibility that $\zeta_\perp = 0$ and $\zeta_y \neq 0$ or $\zeta_\perp \neq 0$ and $\zeta_y = 0$. This describes a *tubular* phase, in which the membrane is crumpled in some internal directions but flat in the remaining ones.[84, 85]. Fig.15 displays a typical equilibrium configuration from the tubular phase, along with the low and high-temperature flat and crumpled phases for a phantom anisotropic membrane.

Let's deal with the phantom anisotropic membrane first. Both analytical[86] and numerical work[87] has established that the phase diagram contains a crumpled, tubular and flat phase. The crumpled and flat phases are equivalent to the isotropic ones, so anisotropy turns out to be an irrelevant interaction in those phases. The new physics is contained in the tubular phase.

A. Phantom Tubular Phase

1. The Phase diagram

We first describe the mean field theory phase diagram and then the effect of fluctuations. There are two situations depending on the value of a certain function Δ, which depends on the elastic constants $u_{\perp\perp}, v_{\perp y}, u_{yy}$ and $v_{\perp\perp}$.[84, 85, 86]

For $\Delta > 0$ the mean field solution exhibits crumpled, flat and tubular phases. When $t_y > 0$ and $t_\perp > 0$ the model is crumpled. Lowering the temperature so that one of the t couplings becomes negative drives the membrane to the tubular phase (either a $\perp$ or y-tubule). Lowering the temperature still further flattens the membrane. For $\Delta < 0$ the flat phase disappears from the mean field solution, leaving only the crumpled and tubular phases separated by a continuous transition. Tubular phases are the stable low temperature stable phases in this regime. This mean field result is summarized in Fig.16.

Beyond mean field theory, the Ginzburg criterion applied to this particular model suggests that the phase diagram is stable for physical membranes $D = 2$ at any embedding dimension d. The mean field description should be qualitative correct even for the full model.

Numerical simulations have spectacularly confirmed this beautiful analytic prediction.[87] Changing the temperature generates a sequence of continuous phase transitions crumpled-to-tubular and tubular-to-flat, in total agreement with the $\Delta > 0$ case above (see Fig.16).

2. The Crumpled Anisotropic Phase

In this phase $t_y > 0$ and $t_\perp > 0$, and the free energy Eq.(39) reduces , for $D \geq 2$, to

$$
F(\vec{r}(\mathbf{x})) = \frac{1}{2} \int d^{D-1}\mathbf{x}_\perp dy \left[t_\perp (\partial_\alpha^\perp \vec{r})^2 + t_y (\partial_y \vec{r})^2 \right] + \text{Irrelevant Terms} \;.
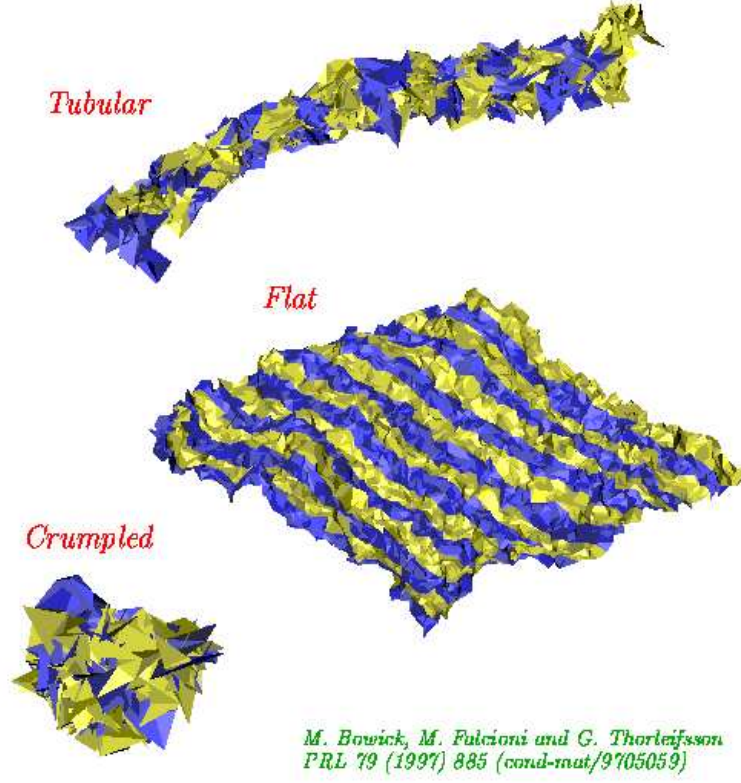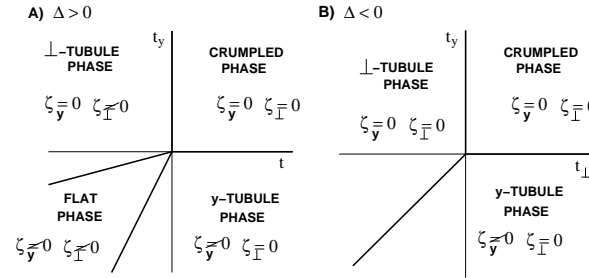\tag{41}
$$

FIG. 15:

FIG. 16: The phase diagram for anisotropic phantom membranes.

By redefining the y coordinate to be $y' = \frac{t_\perp}{t_y} y$ this reduces to Eq.(6), with $t \equiv t_\perp$. Anisotropy is clearly irrelevant in the crumpled phase.

3. The Flat Phase

In the flat phase intrinsic anisotropies are only apparent at short-distances and therefore should be irrelevant in the infrared limit. This argument may be made more precise.[88] The flat phase is thus equivalent to the flat phase of isotropic membranes.

B. The Tubular Phase

We now turn to the study of the novel tubular phase, both in the phantom case and with self-avoidance. Since the physically relevant case for membranes is $D = 2$ the y-tubular and $\perp$-tubular phase are the same.

The key critical exponents characterizing the tubular phase are the size (or Flory) exponent ν, giving the scaling of the tubular diameter R_g with the extended (L_y) and transverse ($L_\perp$) sizes of the membrane, and the roughness exponent ζ associated with the growth of height fluctuations h_{rms} (see Fig.17):

$$R_g(L_\perp, L_y) \ \propto \ L_\perp^\nu S_R(L_y/L_\perp^z) \ ; \tag{42}$$
$$h_{rms}(L_\perp, L_y) \ \propto \ L_y^\zeta S_h(L_y/L_\perp^z) \ ,$$

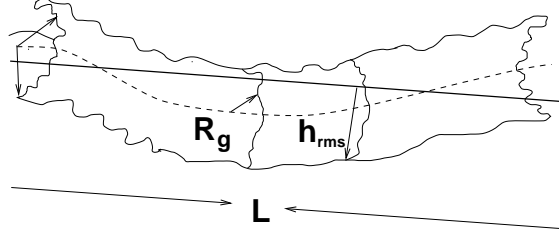where S_R and S_h are scaling functions[84, 85] and z is the anisotropy exponent.

FIG. 17: A schematic illustration of a tubular configuration indicating the radius of gyration R_g and the height fluctuations h_{rms}.

The general free energy described in Eq.(39) may be simplified considerably in a y-tubular phase.[89, 90]:

$$\begin{aligned}
F(u, \vec{h}) \ = \ & \frac{1}{2} \int d^{D-1}\mathbf{x}_\perp dy \left[\kappa(\partial_y^2 \vec{h})^2 + t(\partial_\alpha \vec{h})^2 \right. \\
& + g_\perp(\partial_\alpha u + \partial_\alpha \vec{h} \partial_y \vec{h})^2 \\
& + \left. g_y(\partial_y u + \frac{1}{2}(\partial_y \vec{h})^2)^2 \right] \\
& + \frac{b}{2} \int dy\, d^{D-1}\mathbf{x}_\perp d^{D-1}\mathbf{x}'_\perp \delta^{d-1}(\vec{h}(\mathbf{x}_\perp, y) - \vec{h}(\mathbf{x}'_\perp, y)) \ ,
\end{aligned} \tag{43}$$

reducing the number of free couplings to five. The coupling $g_\perp$, furthermore, is irrelevant by standard power counting. The most natural assumption is to set it to zero. In that case the phase diagram one obtains is shown in Fig.18. Without self-avoidance, i.e. $b = 0$, the Gaussian Fixed Point (GFP) is unstable and the long-wavelength behavior of the membrane is controlled by the tubular phase fixed point (TPFP). Any amount of self-avoidance, however, leads to a new fixed point, the Self-avoiding Tubular fixed point (SAFP), which describes the large distance properties of self-avoiding tubules.

Radzihovsky and Toner advocate a different scenario.[85] For sufficiently small embedding dimensions d, including the physical $d = 3$ case, these authors suggest the existence of a new bending rigidity renormalized fixed point (BRFP), which is the infra-red fixed point describing the actual properties of self-avoiding tubules (see Fig. 19).

Here we follow the arguments presented in Refs.[89, 90] and consider the model defined by Eq.(43) with the $g_\perp$-term set to zero. One can prove then than there are some general scaling relations among the critical exponents. All three exponents may be expressed in terms of a single exponent

$$\zeta \ = \ \frac{3}{2} + \frac{1-D}{2z} \ ; $$
$$\nu \ = \zeta z \ . \tag{44}$$

Remarkably, the phantom case, as described by Eq.(43), can be solved exactly. The result for the size exponent is

$$\nu_{ph}(D) = \frac{5 - 2D}{4} \ , \ \nu_{ph}(2) = \frac{1}{4} \tag{45}$$

FIG. 18: The phase diagram for self-avoiding anisotropic membranes with the Gaussian fixed point (GFP), the tubular phase fixed point (TPFP) and the self-avoidance fixed point (SAFP).
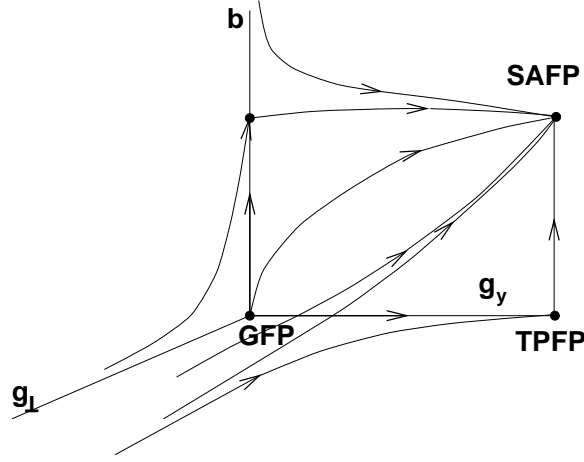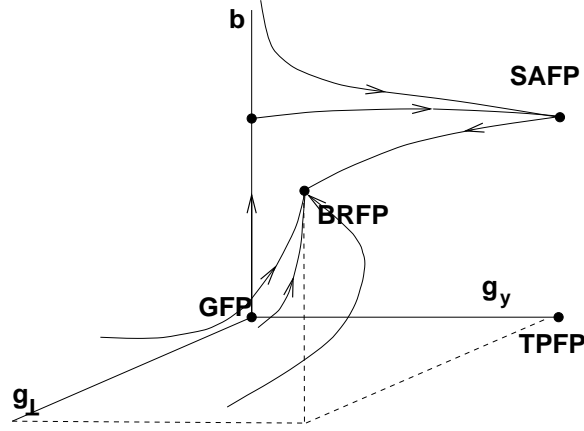

FIG. 19: The phase diagram for self-avoiding anisotropic membranes with the Gaussian fixed point (GFP), the tubular phase fixed point (TPFP), the self-avoidance fixed point (SAFP) and the bending rigidity fixed point (BRFP).

with the remaining exponents following from the scaling relations Eq.(44).

The self-avoiding case may be treated with techniques similar to those in isotropic case. The size exponent may be estimated within the Flory approximation, yielding

$$\nu_{Fl} = 2/d_H = \frac{D+1}{d+1} \ . \tag{46}$$

The Flory estimate is an uncontrolled approximation. Fortunately, a ε-expansion, adapting the multi-local operator product expansion technique[91]$^-$[93] to the case of tubules, is also possible.[89, 90] The resulting renormalization group β-functions provide evidence for the phase diagram shown in Fig.18. Extrapolation techniques also provide estimates for the size exponent, the most accurate value being $\nu = 0.62$ for the physical case. The rest of the exponents may be computed from the scaling relations.

Numerical simulations so far, however, do *not* find a tubular phase in the case of strict self-avoidance.

VI.   ORDER ON CURVED SURFACES

Imagine we instantaneously freeze a fluctuating membrane so that it has some fixed but curved shape. We can then ask about the nature of the ground state of particles distributed on this surface and interacting with some microscopic

pair-wise repulsive potential. The relevant physics is clearly related to the infinite bending rigidity limit (flat phase) of elastic membranes. In such a membrane the topology and topography are fixed.
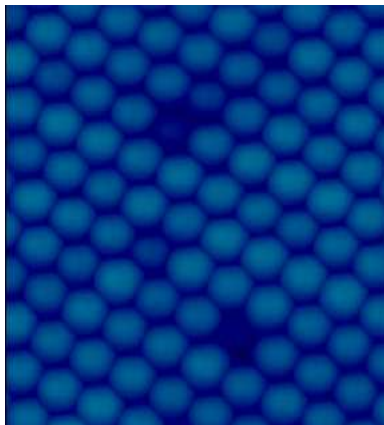

FIG. 20: A 2.5 micron scan of 0.269 micron diameter polystyrene spheres crystallized into a regular triangular lattice - taken from http://invsee.asu.edu/nmodules/spheresmod/.

Spherical particles on a flat surface pack most efficiently in a simple triangular lattice, as illustrated in Fig.20. In the dense limit each particle "kisses" six of its neighbors.[94] Such six-coordinated triangular lattices cannot, however, be perfectly wrapped on the curved surface of a sphere; topology alone requires there be defects in coordination number. The panels on a soccer ball and the spherical carbon molecule C_{60} (buckyball)[97, 98] are good illustrations of the necessity of defects for a spherical triangulation – they have 12 pentagonal faces (each the dual of a 5-coordinated defect) in addition to 20 hexagonal faces (each dual to a regular 6-coordinated node.) The necessary packing defects can be characterized by their topological charge, q, which is the departure of their coordination number c from the preferred flat space value of 6 ($q = 6 - c$). These coordination number defects are point-like topological defects called *disclinations*[99] and they detect intrinsic Gaussian curvature located at the defect. A profound theorem of Euler[100, 101] states that the total disclination charge of *any* triangulation whatsoever of the sphere must be 12![102] A total disclination charge of 12 can be achieved in many ways, however, which makes the determination of the minimum energy configuration of repulsive particles, essential for crystallography on a sphere, an extremely difficult problem. This was recognized nearly 100 years ago by J.J. Thomson[103], who attempted, unsuccessfully, to explain the periodic table in terms of rigid electron shells. Similar problems arise in fields as diverse as multi-electron bubbles in superfluid helium,[104] virus morphology,[105]−[108] protein s-layers,[109, 110] giant molecules[111, 112] and information processing.[95, 96] Indeed, both the classic Thomson problem, which deals with particles interacting through the Coulomb potential, and its generalization to other interaction potentials, are still open problems after almost 100 years of attention.[113]− [115]

The spatial curvature encountered in curved geometries adds a fundamentally new ingredient to crystallography not found in the study of order in spatially flat systems. As the number of particles on the sphere grows, isolated charge 1 defects (5s) will induce too much strain. This strain can be relieved by introducing additional dislocations, consisting of pairs of tightly bound 5-7 defects[116, 117], which don't spoil the topological constraints because their net disclination charge is zero. Dislocations, which are themselves point-like topological defects in two dimensions, disrupt the translational order of the crystalline phase but are less disruptive of orientational order.[117]

Recent work on an experimental realization of the generalized Thomson problem has allowed us to explore the lowest energy configuration of the dense packing of repulsive particles on a spherical surface and to confront a previously developed theory with experiment.[118]. We create two-dimensional packings of colloidal particles on the surface of spherical water droplets and view the structures with optical microscopy. Above a critical system size, the thermally equilibrated colloidal crystals display distinctive high-angle grain boundaries, which we call "scars". These grain boundaries are found to end entirely within the crystal, which is never observed on flat surfaces because the energy penalty is too high.

The experimental system is based on the self-assembly of one micron diameter cross-linked polystyrene beads adsorbed on the surface of spherical water droplets (of radius R), themselves suspended in a density-matched oil mixture.[119] The polystyrene beads are almost equally happy to be in oil or water (the bead/oil surface tension is close to the bead/water surface tension) and therefore diffuse freely *until* they find the oil-water interface and stick there. Particle assembly on the interface of two distinct liquids dates to the pioneering work of Pickering[120] and was beautifully exploited by Pieranski[121] some time ago. The particles are imaged with phase contrast using an

inverted microscope. After determining the center of mass of each bead, the lattice geometry is analyzed by original Delaunay triangulation algorithms[122] appropriate to spherical surfaces.
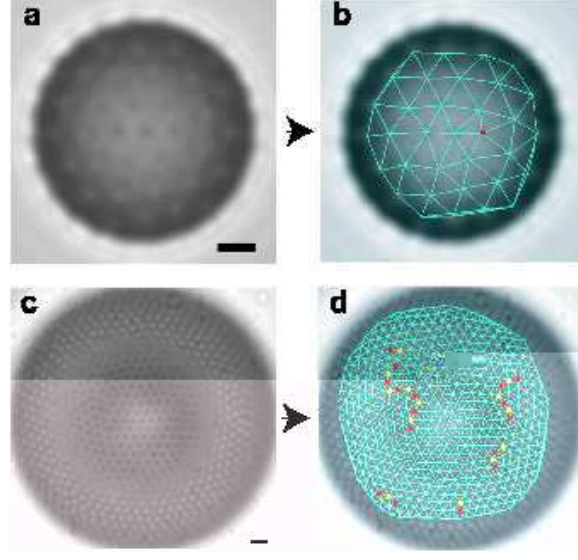

FIG. 21: Light microscope images of particle-coated droplets. Two droplets (**A**) and (**C**) are shown, together with their associated defect structures (**B**) and (**D**). Panel (**A**) shows an $\approx 13\%$ portion of a small spherical droplet with radius $R = 12.0$ microns and mean particle spacing $a = 2.9$ microns (R/a = 4.2), along with the associated triangulation (**B**). Charge $+1(-1)$ disclinations are shown in red and yellow respectively. Only one $+1$ disclination is seen. Panel (**C**) shows a cap of spherical colloidal crystal on a water droplet of radius $R = 43.9$ microns with mean particle spacing $a = 3.1$ microns (R/a = 14.3), along with the associated triangulation (**D**). In this case the imaged crystal covers about 17% of the surface area of the sphere. The scale bars in (**A**) and (**C**) are 5 microns.

We analyze the lattice configurations of a collection of 40 droplets. A typical small spherical droplet with system size, R/a = 4.2, where a is the mean particle spacing, is shown in Fig. 21**A**. The associated Delaunay triangulation is shown in Fig. 21**B**. The only defect is one isolated charge $+1$ disclination. Extrapolation to the entire surface of the sphere is statistically consistent with the required 12 total disclinations.

Qualitatively different results are observed for larger droplet sizes as defect configurations with excess dislocations appear. Although some of these excess dislocations are isolated, most occur in the form of distinctive $(5-7-5-7-\cdots-5)$ chains, each of net charge $+1$, as shown in Fig. 21**D**. These chains form high-angle ($30°$) grain boundaries, or scars, which terminate freely within the crystal. Such a feature is energetically prohibitive in equilibrium crystals in flat space. Thus, although grain boundaries are a common feature of 2D and 3D crystalline materials, arising from a mismatch of crystallographic orientations across a boundary, they usually terminate at the boundary of the sample in flat space because of the excessive strain energy associated with isolated terminal disclinations. Termination within the crystal is a feature unique to curved space.

Of key interest is the number of excess dislocations per chain as a function of the dimensionless system size R/a. This is plotted in Fig. 22. Scars only appear for droplets with R/a ≥ 5. These results provide a critical confirmation of a theoretical prediction that R/a must exceed a threshold value $(R/a)_c \approx 5$, corresponding to $M \approx 360$ particles, for excess defects to proliferate in the ground state of a spherical crystal.[123] The precise value of $(R/a)_c$ depends on details of the microscopic potential, but its origin is easily understood by considering just one of the 12 charge $+1$ disclinations required by the topology of the sphere. In flat space such a topological defect has an associated energy that grows quadratically with the size of the system,[117] since it is created by excising a $2\pi/6$ wedge of material and gluing the boundaries together.[11, 117] The elastic strain energy associated with this defect grows as the area. In the case of the sphere the radius plays the role of the system size. As the radius increases, isolated disclinations become much more energetically costly. This elastic strain energy may be reduced by the formation of linear dislocation arrays, i.e. grain boundaries. The energy needed to create these additional dislocation arrays is proportional to a dislocation core energy E_c and scales linearly with the system size.[123] Such screening is inevitable in flat space (the plane) if one forces an extra disclination into the defect-free ground state. Unlike the situation in flat space, grain boundaries on the sphere can freely terminate,[123]$^-$[126] consistent with the scars seen on colloidal droplets.

A powerful analytic approach to determining the ground state of particles distributed on a curved surface has been developed.[123, 126, 127] The original particle problem is mapped to a system of interacting disclination defects in a continuum elastic curved background. The defect-defect interaction is universal with the particle microscopic
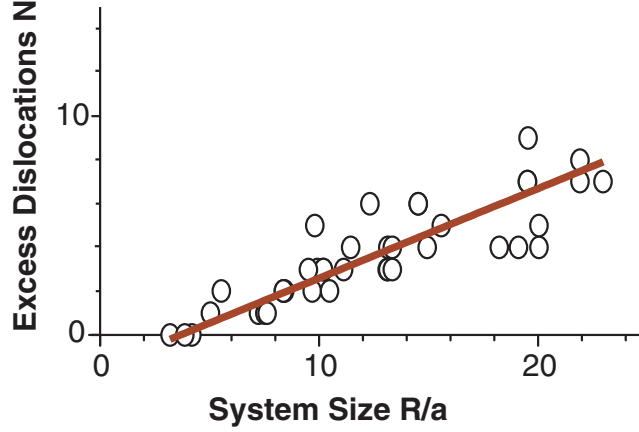
FIG. 22: Excess dislocations as a function of system size. The number of excess dislocations per minimal disclination N as a function of system size R/a, with the linear prediction given by theory shown as a solid red line.

potential determining two free parameters – the Young modulus K_0 of the elastic background and the core energy E_c of an elementary disclination. A rigorous geometrical derivation of the effective free energy for the defects is given in Ref.[128] An equivalent derivation may also be given by integrating out the phonon degrees of freedom from the elastic Hamiltonian,[29] with the appropriate modifications for a general distribution of defects. The energy of a two-dimensional crystal embedded in an arbitrary frozen geometry described by a metric $g_{ij}(\mathbf{x})$ is given by

$$
\begin{aligned}
H = \ & E_0 \ + \frac{Y}{2} \int \int d\sigma(x) d\sigma(y) \\
& \times \ \left\{ [s(x) - K(x)] \frac{1}{\Delta^2} [(s(y) - K(y))] \right\} \ ,
\end{aligned}
\tag{47}
$$

where the integration is over a fixed surface with area element $d\sigma(x)$ and metric g_{ij}, K is the Gaussian curvature, Y is the Young modulus in flat space and $s(x) = \sum_{i=1}^{N} \frac{\pi}{3} q_i \delta(x, x_i)$ is the disclination density $\left[\delta(x, x_i) = \delta(x - x_i)/\sqrt{det(g_{ij})} \right]$. Here 5- and 7-fold defects correspond to $q_i = +1$ and -1, respectively. Defects like dislocations or grain boundaries can be built from these N elementary disclinations. E_0 is the energy corresponding to a perfect defect-free crystal with no Gaussian curvature; E_0 would be the ground state energy for a 2D Wigner crystal of electrons in the plane.[129] Eq.(47), restricted to a sphere, gives[123]

$$
\begin{aligned}
H = E_0 \ + \ & \frac{\pi Y}{36} R^2 \sum_{i=1}^{N} \sum_{j=1}^{N} q_i q_j \chi(\theta^i, \psi^i; \theta^j, \psi^j) \\
+ \ & N E_c \ ,
\end{aligned}
\tag{48}
$$

where E_c is a defect core energy, R is the radius of the sphere and χ is a function of the geodesic distance β_{ij} between defects with polar coordinates $(\theta^i, \psi^i \ ; \ \theta^j, \psi^j)$:

$$
\chi(\beta) = 1 + \int_0^{\frac{1 - \cos \beta}{2}} dz \, \frac{\ln z}{1 - z} \ .
\tag{49}
$$

The potential is attractive for opposite charged defects and repulsive for like-charged defects. Many predictions of this model are universal in the sense that they are insensitive to the microscopic potential. This enables us to make definite predictions even though the colloidal potential is not precisely known. It also means that our model system serves as a prototype for any analogous system with repulsive interactions and spherical geometry. To further test the validity of this approach, we show a typical ground state for large M in Fig. 23. The system size here is R/a = 12, similar to the droplet in Fig. 21**D**. The results are remarkably similar to the experimentally observed configuration in Fig. 21**D**; the only difference is a result of thermal fluctuations, which break the two defect scars in the experiment. This agreement
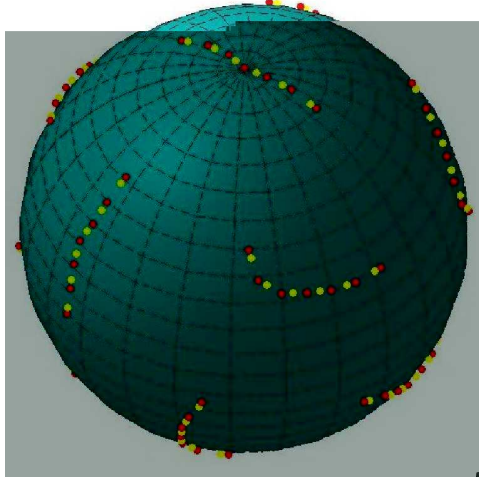
FIG. 23: Model grain boundaries. This image is obtained from a numerical minimization for a system size comparable to the large droplet in Fig.21(**c**,**d**).
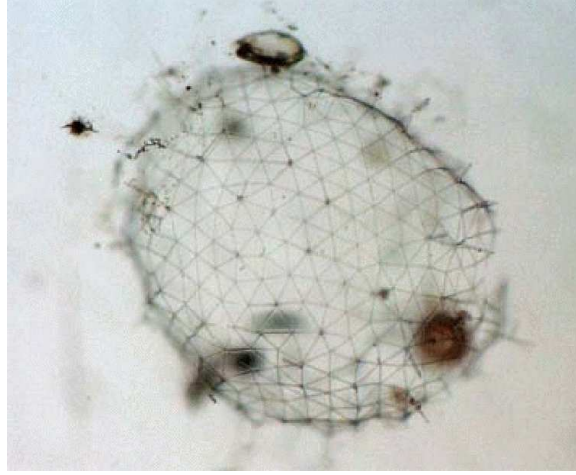

FIG. 24: The polyhedral siliceous cytoskeleton of the unicellular ocean organism *Aulosphaera*.

between theory and experiment also provides convincing evidence that these scars are essential components of the equilibrium crystal structure on a sphere.

The theory predicts that an isolated charge $+1$ disclination on a sphere is screened by a string of dislocations of length $\cos^{-1}(5/6)R \approx 0.59R$.[123] One can use the variable linear density of dislocations to compute the total number of excess dislocations N in a scar. One finds that N grows for large (R/a) as $\frac{\pi}{3}\left[\sqrt{11} - 5\cos^{-1}(5/6)\right]\frac{\text{R}}{\text{a}} \approx 0.41\frac{\text{R}}{\text{a}}$, independently of the microscopic potential. This prediction is universal, and is in remarkable agreement with the experiment, as shown by the solid line in Fig. 22.

We expect these scars to be widespread in nature. They should occur, and hence may be exploited, in sufficiently large stiff viral protein capsids, giant spherical fullerenes, spherical bacterial surface layers (s-layers), provided that the spherical geometry is not too distorted. Terminating strings of heptagons and pentagons might serve as sites for chemical reactions or even initiation points for bacterial cell division[109] and will surely influence the mechanical properties of spherical crystalline shells.

The polyhedral siliceous cytoskeleton of the unicellular non-motile ocean organism *Aulosphaera* (a member of the species *Phaeodaria*[130]) is shown in Fig.24. A triangulation revealing three scars, two of which are branched, is shown in Fig.25. The skeleton itself is such a perfect triangular lattice that it coincides with the Delaunay triangulation determined by its vertices. The case of viral capsids has been analyzed in Ref.[108], where it is shown that, rather than scarring, icosahedral packings become unstable to faceting for sufficiently large virus size, in analogy with the buckling instability of disclinations in two-dimensional crystals.[5, 131]
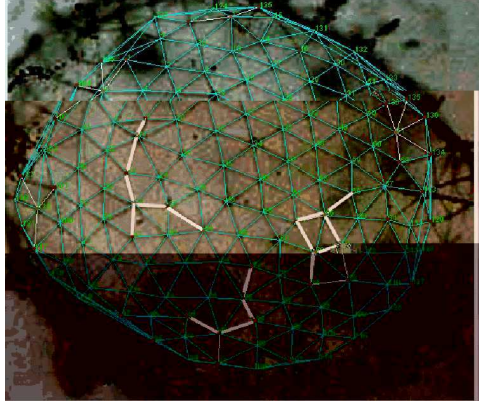
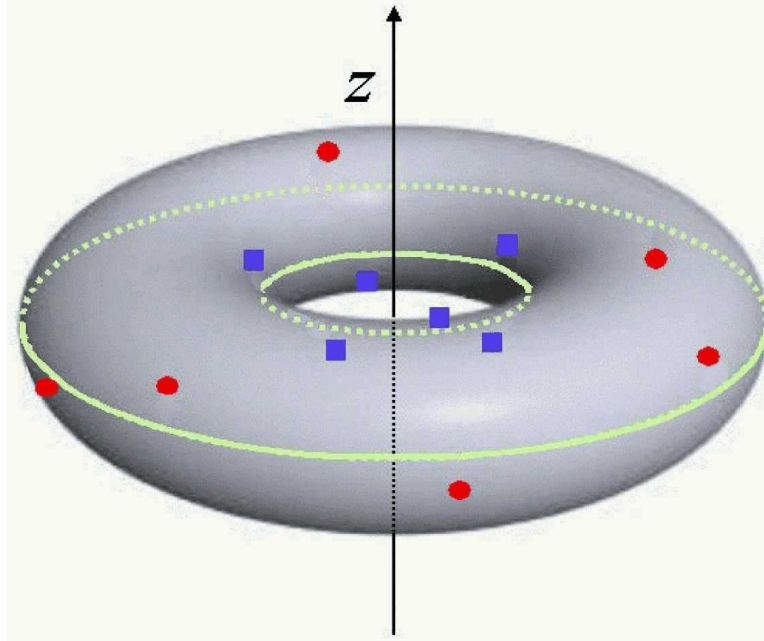FIG. 25: The Delaunay triangulation of the *Aulosphaera* cytoskeleon above.

FIG. 26: A typical ground state for a toroidal hexatic. Five-fold disclinations are shown as solid circles (red) and 7-fold disclinations as solid squares (blue).

Scarred spherical crystals may provide the building blocks (atoms) of micron-scale molecules[132, 133] and materials. While topology dictates the overall number of scars (12), the details of the geometry and defect energetics determine the length and structure of the scars themselves. It is possible that scarred colloidosomes will ultimately yield complex self-assembled materials with novel mechanical or optoelectronic properties.[132]

New structures arise if one changes the structure of the colloid of the topology of the surface they coat. Nelson has analyzed the case of nematic colloids coating a sphere.[133] In this case the preferred number of elementary disclination defects is 4, allowing for the possibility of colloidal atoms with tetrahedral functionality and sp^3-type bonding. The case of toroidal templates with 6-fold bond-orientational (hexatic) order has been analyzed recently.[127] It is found that defects are energetically favored in the ground state for fat torii or moderate vesicle size. A schematic of a "typical" ground state is shown in Fig.26.

VII. ACKNOWLEGMENTS

Guitter and Gudmar Thorleifsson.

[1] P. G. de Gennes, *Scaling Concepts in Polymer Physics* (Cornell University Press, Ithaca, NY, 1979).
[2] G. des Cloiseaux and J.F. Jannink, *Polymers in Solution: Their Modelling and Structure* (Clarendon Press, Oxford, 1990).
[3] P.G. de Gennes and J. Badoz, *Fragile objects* (Copernicus, Springer-Verlag, New York, 1996).
[4] Y. Kantor, "Properties of Tethered Surfaces," (this volume).
[5] D.R. Nelson and L. Peliti, *J. Phys. (France)* **48**, 1085 (1987).
[6] See F. David, *Geometry and Field Theory of Random Surfaces and Membranes*, this volume.
[7] D. R. Nelson, "Defects in superfluids, superconductors and membranes," in *Fluctuating Geometries in Statistical Mechanics and Field Theory,* edited by F. David, P. Ginsparg and J. Zinn-Justin (North Holland, Amsterdam, 1966), pp.423-477.
[8] "Gego's Galaxies: Setting Free the Line", R. Storr, *Art in America*, 108-113 (June, 2003).
[9] M. J. Bowick and A. Travesset, "The Statistical Mechanics of Membranes", *Phys. Rep.* **344**, 255–310 (2001); in "Renormalization Group Theory at the Turn of the Millennium," eds. D. O'Connor and C.R. Stephens [arXiv:cond-mat/0002038].
[10] K.J. Wiese, *Polymerized Membranes, a Review*, in "Phase Transitions and Critical Phenomena," Vol. **19**, 253: C. Domb and J.L. Lebowitz (Eds.), Academic Press (2001).
[11] P. M. Chaikin and T. C. Lubensky, *Principles of Condensed Matter Physics* (Cambridge University Press, Cambridge, 1995).
[12] T.C. Lubensky, *Solid State Commun.* **102**, 187 (1997) [arXiv:cond-mat/9609215].
[13] T. A. Witten, *Rev. Mod. Phys.* **71**, S367 (1999).
[14] S. I. Stupp, S. Son, H. C. Lin and L. S. Li, *Science* **259**, 59 (1993).
[15] J. H. Fendler and P. Tundo, *Acc. Chem. Res.* **17**, 3 (1984).
[16] J. H. Fendler, *Chem. Rev.* **87**, 877 (1987).
[17] See Chapter 10 of B. Alberts, D. Bray, J. Lewis, M. Raff, K. Roberts and J. D. Watson, *Molecular Biology of the Cell* (Garland Publishing, New York, 1994).
[18] *Structure and Dymanics of Membranes*, Handbook of Biological Physics Vol. 1, edited by R. Lipowsky and E. Sackmann (Elsevier, Amsterdam, 1995).
[19] C. Picart and D. E. Discher, *Biophys. J.* **77**, 865 (1999).
[20] E. Sackmann, *ChemPhysChem* **3**, 237 (2002).
[21] D. Boal, *Mechanics of the Cell* (Cambridge University Press, Cambridge, UK, 2002).
[22] T. J. Byers and D. Branton, *Proc. Nat. Acad. Sci. U.S.A.* **82**, 6153 (1985).
[23] A. Elgsaeter, B. T. Stokke, A. Mikkelsen and D. Branton, Science **234**, 1217 (1986).
[24] C. F. Schmidt, K. Svoboda, N. Lei, I. B. Petsche, L. E. Berman, C. R. Safinya and G. S. Grest, Science **259**, 952 (1993).
[25] T. Hwa, E. Kokufuta and T. Tanaka, *Phys. Rev.* **A44**, R2235 (1991).
[26] X. Wen et. al., *Nature* **355**, 426 (1992).
[27] M.S. Spector, E. Naranjo, S. Chiruvolu and J. A. Zasadzinski, *Phys. Rev. Lett.* **73**, 2867 (1994).
[28] R. R. Chianelli, E. B. Prestridge, T. A. Pecoraro and J. P. DeNeufville, *Science* **203**, 1105 (1999).
[29] See D.R. Nelson, *The Theory of the Crumpling Transition*, this volume.
[30] M. Paczuski, M. Kardar and D.R. Nelson, *Phys. Rev. Lett.* **60**, 2638 (1988).
[31] M. J. Bowick, S. M. Catterall, M. Falcioni, G. Thorleifsson and K. N. Anagnostopoulos, *J. Phys. I (France)* **6**, 1321 (1996) [arXiv:cond-mat/9603157].
[32] K. Wilson and J. Kogut, *Phys. Rep.* **12**, 75 (1974).
[33] N. Goldenfeld, *Lectures on Phase Transitions and the Renormalization Group* (Westview Press, 1992).
[34] Y. Kantor, M. Kardar and D.R. Nelson, *Phys. Rev. Lett.* **57**, 791 (1986).
[35] Y. Kantor, M. Kardar and D.R. Nelson, *Phys. Rev.* **A35**, 3056 (1987).
[36] See B. Duplantier, this volume.
[37] M. Baig, D. Espriu and J. Wheater, *Nucl. Phys.* **B314**, 587 (1989).
[38] J. Ambjørn, B. Durhuus and T. Jonsson, *Nucl. Phys.* **B316**, 526 (1989).
[39] R. Renken and J. Kogut, *Nucl. Phys.* **B342**, 753 (1990).
[40] R. G. Harnish and J. Wheater, *Nucl. Phys.* **B350**, 861 (1991).
[41] J. Wheater and T. Stephenson, *Phys. Lett.* **B302**, 447 (1993).
[42] M. Baig, D. Espriu and A. Travesset, *Nucl. Phys.* **B426**, 575 (1994).
[43] J. Wheater, *Nucl. Phys.* **B458**, 671 (1996).
[44] G. Gompper and D. M. Kroll, *J. Phys.: Condens. Matter* **9**, 8795 (1997).
[45] G. Gompper and D. M. Kroll, *Curr. Opin. Colloid Interface Sci.* **2**, 373 (1997).
[46] F. David and E. Guitter, *Europhys. Lett.* **5**, 709 (1988).
[47] E. Guitter, F. David, S. Leibler and L. Peilit, *Phys. Rev. Lett.* **61**, 2949 (1988); *J. Phys. France* **50**, 1787 (1989).
[48] P. Le Doussal and L. Radzihovsky, *Phys. Rev. Lett.* **69**, 1209 (1992).
[49] D. Espriu and A. Travesset, *Nucl. Phys.* **B468**, 514 (1996).

[50] L. D. Landau and E. M. Lifshitz, *Theory of Elasticity*, Vol. **7** of *Course of Theoretical Physics* (Pergamon Press, Oxford, UK, 1986).

[51] J.A. Aronovitz and T.C. Lubensky, *Phys. Rev. Lett.* **60**, 2634 (1988).

[52] J. A. Aronovitz, L. Golubović and T. C. Lubensky, *J. Phys. France* **50**, 609 (1989).

[53] Z. Zhang, H.T. Davis and D.M. Kroll, *Phys. Rev.* **E53**, 1422 (1996).

[54] M. Falcioni, M. J. Bowick, E. Guitter and G. Thorleifsson, *Europhys. Lett.* **38**, 67 (1997) [arXiv:cond-mat/9610007].

[55] K. E. Evans, M. A. Nkansah, I. J. Hutchinson and S. C. Rogers, Nature **353**, 124 (1991).

[56] M. Plischke and D. Boal, *Phys. Rev.* **A38**, 4943 (1988).

[57] F. F. Abraham, W. Rudge and M. Plischke, *Phys. Rev. Lett.* **92**, 1757 (1989).

[58] F. F. Abraham and D. R. Nelson, *J. Phys. France* **51**, 2653 (1990).

[59] F. F. Abraham and D.R. Nelson, *Science* **249**, 393 (1990).

[60] B. Boal, E. Levinson, D. Liu and M. Plischke, *Phys. Rev.* **A40**, 3292 (1989).

[61] Y. Kantor and K. Kremer, *Phys. Rev.* **E48**, 2490 (1993).

[62] M. Bowick, A. Cacciuto, G. Thorleifsson and A. Travesset, *Eur. Phys. J.* **E5**, 149 (2001) [arXiv:cond-mat/0006383].

[63] A. Baumgartner, *J. Phys. I France* **1**, 1549 (1991).

[64] D. M. Kroll and G. Gompper, *J. Phys. France* **3**, 1131 (1993).

[65] P. Di Francesco and E. Guitter, *Europhys. Lett.* **26**, 455 (1994) [arXiv:cond-mat/9402058].

[66] P. Di Francesco and E. Guitter, *Phys. Rev.* **E50**, 4418 (1994) [arXiv:cond-mat/9406041].

[67] M. Bowick, P. DiFrancesco, O. Golinelli and E. Guitter, *Nucl. Phys.* **B450**, 463 (1995) [arXiv:cond-mat/9502063].

[68] M. Bowick, P. DiFrancesco, O. Golinelli and E. Guitter, p.21 in *Common trends in Condensed Matter and High Energy Physics*; eds. A. Barone and A. Devoto (Istituto Italiano per gli Studi Filosofici, Naples, 2000) [arXiv:cond-mat/9610215].

[69] M. Bowick. O. Golinelli, E. Guitter and S. Mori, *Nucl. Phys.* **B495**, 583 (1997) [arXiv:cond-mat/99611105].

[70] E. Cirillo, G. Gonnella and A. Pelizzola, *Phys. Rev.* **E53**, 1479 (1996) [arXiv:hep-th/9507160].

[71] E. Cirillo, G. Gonnella and A. Pelizzola, *Phys. Rev.* **E53**, 3253 (1996) [arXiv:hep-th/9512069].

[72] G. Grest, *J. Phys. I (France)* **1**, 1695 (1991).

[73] M. Bowick, A. Cacciuto, G. Thorleifsson and A. Travesset, *Phys. Rev. Lett* **87**, 148103 (2001) [arXiv:cond-mat/0103173].

[74] Poisson himself "proved" that the Poisson ratio must be $\frac{1}{4}$ for an elastic cylinder under tension, based on a faulty molecular-force model due to Laplace and the neglect of shear forces [76].

[75] A.E.H. Love, *A Treatise on the Mathematical Theory of Elasticity* (Dover, New York, 1944), 4th edition, p.163.

[76] *Siméon-Denis Poisson et La Science de son Temps*, M. Métivier, P. Costabel and P. Dugac (L'Ecole Polytechnique Press, Palaiseau, France, 1981).

[77] R. Lakes, Science **235**, 1038 (1987).

[78] For more details, including a recipe for making auxetic foam, see http://silver.neep.wisc.edu~lakes/Poisson.html.

[79] K. E. Evans and A. Alderson, Adv. Mater. **12**, 617 (2000).

[80] A. Yeganeh-Haeri, D. J. Weidner, and J. B. Parise, Science **257**, 650 (1992).

[81] N. Keskar and J. R. Chelikowsky, Nature (London) **358**, 222 (1992).

[82] D. E. Discher, N. Mohandas and E. A. Evans, Science **266**, 1032 (1994).

[83] R. Lakes, Nature (London) **414**, 503 (2001).

[84] L. Radzihovsky and J. Toner, *Phys. Rev. Lett.* **75**, 4752 (1995) [arXiv:cond-mat/9510172].

[85] L. Radzihovsky and J. Toner, *Phys. Rev.* **E57**, 1832 (1998) [arXiv:cond-mat/9708046].

[86] See L. Radzihovsky, this volume.

[87] M. Bowick, M. Falcioni and G. Thorleifsson, *Phys. Rev. Lett.* **79**, 885 (1997) [arXiv:cond-mat/9708046].

[88] J. Toner, *Phys. Rev. Lett.* **62**, 905 (1988).

[89] M. Bowick and E. Guitter, *Phys. Rev.* **E56**, 7023 (1997) [arXiv:cond-mat/9705045].

[90] M. Bowick and A. Travesset, *Phys. Rev.* **E59**, 5659 (1999) [arXiv:cond-mat/9808214].

[91] B. Duplantier, T. Hwa and M. Kardar, *Phys. Rev. Lett.* **70**, 2205 (1993) [arXiv:hep-th/9212102].

[92] F. David, B. Duplantier and E. Guitter, *Nucl. Phys.* **B394**, 555 (1993) [arXiv:hep-th/9211038].

[93] F. David, B. Duplantier and E. Guitter, arXiv:cond-mat/9702136.

[94] The kissing number for sphere packings in 3 dimensions is 12, in 8 dimensions 240 and in 24 dimensions 196,650.[95, 96]

[95] N.J.A. Sloane, *Sci. Am.* **250**, 116 (1984).

[96] J.H. Conway and N.J.A. Sloane, *Sphere Packings, Lattices and Groups* (Third Edition, Springer-Verlag, New York, 1998).

[97] H.W. Kroto *et al.*, *Nature* **318**, 162 (1985).

[98] M.F. Jarrold, *Nature* **407**, 26 (2000).

[99] See F. David, this volume.

[100] L. Euler, *Opera Omnia*, series i, Vol. **26**, Orell Füssli Verlag, 1953 (see also http://www.ics.uci.edu/~eppstein/junkyard/euler/).

[101] P. Hilton, J. Pedersen, *Amer. Math. Monthly* **103**, 121 (1996).

[102] 12 here is obtained from 6χ, where the Euler characteristic χ of a space is a topological invariant equal to 2 for the sphere.

[103] J.J. Thomson, *Phil. Mag.* **7**, 237 (1904).

[104] P. Leiderer, *Z. Phys. B* **98**, 303 (1995).

[105] D.L.D. Caspar, A. Klug, *Cold Spring Harbor Symposia on Quantitative Biology* Vol. **XXVII** (Basic Mechanisms in Animal Virus Biology), 1 (1962).

[106] C.J. Marzec, L.A. Day, *Biophys. Jour.* **65**, 2559 (1993).

[107] V.J. Reddy *et al.*, *J. Virol.* **75**, 11943 (2001) (see also http://mmtsb.scripps.edu/viper/viper.html).

[108] J. Lidmar, L. Mirny and D.R. Nelson, arXiv:cond-mat/0306741.

[109] U.B. Sleytr, M. Sára, D. Pum, B. Schuster, *Prog. Surf. Sci.* **68**, 231 (2001).

[110] D. Pum, P. Messner and U.B. Sleytr, *J. Bacteriology* **173**, 6865 (1991).

[111] T. Liu, J. Am. Chem. Soc. **124**, 10942 (2002).

[112] A. Müller, P. Kögerler and A.W.M. Dress, *Coord. Chem. Rev.* **222**, 193 (2001).

[113] The determination of the aymptotics of the ground state energy of spherical crystals with a logarithmic potential appeared as Problem **7** of Smale's list of key mathematical problems for the 21st century: S. Smale, *Math. Intelligencer* **20**, No. 2, 7 (1998).

[114] E.L. Altschuler *et. al.*, *Phys. Rev. Lett.* **78**, 2681 (1997).

[115] T. Erber, G.M. Hockney, *Advances in Chemical Physics* (eds I. Prigogine, S.A. Rice) Vol. **XCVIII**, 495 (1997).

[116] R. Cotterill, *The Cambridge Guide to the Material World* (Cambridge University Press, Cambridge, England, 1985).

[117] D.R. Nelson, *Defects and Geometry in Condensed Matter Physics*, (Cambridge University Press, Cambridge, 2002).

[118] A.R. Bausch, M.J. Bowick, A. Cacciuto, A.D. Dinsmore, M.F. Hsu, D.R. Nelson, M.G. Nikolaides, A. Travesset and D.A. Weitz, *Science* **299**, 1716 (2003) [arXiv:cond-mat/0303289].

[119] A.D. Dinsmore *et. al.*, *Science* **298**, 1006 (2002); the particular system we explored is obtained by confining cross-linked polystyrene beads (IDC, Portland, USA) to the surface of water droplets.

[120] S. U. Pickering, *J. Chem. Soc.* **97**, 2001 (1907).

[121] P. Pieranski, *Phys. Rev. Lett.* **45**, 569 (1980).

[122] B. Delaunay, *Bull. Acad. Sci. USSR: Class. Sci. Math. Nat.* **7**, 793 (1934).

[123] M.J. Bowick, D.R. Nelson and A. Travesset, *Phys. Rev.* B **62**, 8738 (2000) [arXiv:cond-mat/9911379].

[124] M.J.W. Dodgson and M.A. Moore, *Phys. Rev.* B **60**, 3816 (1997).

[125] A. Perez-Garrido and M.A. Moore, *Phys. Rev.* B **60**, 15628 (1999) and references therein.

[126] M. Bowick, A. Cacciuto, D.R. Nelson, A. Travesset, *Phys. Rev. Lett.* **89**, 185502 (2002) [arXiV:cond-mat/0206144].

[127] M. Bowick, D.R. Nelson and A. Travesset, arXiv:cond-mat/0309709.

[128] M. Bowick and A. Travesset, J. Phys. **A34**, 1535 (2001) [arXiv:cond-mat/0005356].

[129] For the case of a Coulomb potential, see L. Bonsall, A.A. Maradudin, *Phys. Rev. B* **15**, 1959 (1977).

[130] O.R. Anderson, *Radiolaria* (Springer-Verlag, New York, 1983).

[131] S. Seung and D.R. Nelson, Phys. Rev. **A38**, 1005 (1988).

[132] R. Kamien, Science **299**, 1671 (2003).

[133] D.R. Nelson, Nano Lett. **2**, 1125 (2002).